Lawrence Livermore National Laboratory

Assessing the impact of climate change on rain- fall-triggered landslides: a case study in California

S Semnani, Y Han, C Bonfils, J White

September 2025

Landslides

LLNL-JRNL-2011572

Disclaimer

This work performed under the auspices of the U.S. Department of Energy by Lawrence Livermore National Laboratory under Contract DE-AC52-07NA27344.

Technical Note

Landslides (2025) 22:1707–1724
DOI 10.1007/s10346-024-02428-0
Received: 29 August 2024
Accepted: 21 November 2024
Published online: 8 January 2025

Shabnam J. Semnani · Yi Han · Céline J. Bonfils · Joshua A. White

Assessing the impact of climate change on rainfall-triggered landslides: a case study in California

Abstract Landslides are widespread natural hazards which take a heavy toll on lives, property, and infrastructure each year. In January 2023 and 2024, widespread landslides occurred in California as a result of extreme winter precipitation. Estimating the regional evolution of landslide hazard in a changing climate is essential for adaptation planning and risk mitigation efforts. The complex effects of climate change on landslide hazard, however, are poorly understood. Here, we use climate and landslide observations to develop a novel data-driven approach for landslide susceptibility assessment under historical and future climate conditions. We apply this framework to investigate the evolution of landslide susceptibility in California and its impacts on the roadway system based on downscaled climate projections under moderate and high greenhouse gas emission scenarios. On average, the results indicate an increase in landslide susceptibility through 2100 in regions where historical susceptibility is moderate to very high. Although the spatio-temporal variations in landslide susceptibility are sensitive to climate model uncertainties in predicting extreme rainfall, the direst impacts are largely circumvented in lower emission scenarios.

Keywords Landslides · Climate change · Climate adaptation · Susceptibility mapping · Machine learning

Introduction

In the coastal and mountainous areas of California, environmental shifts resulting from climate change have led to increased risk of several natural hazards—including drought, wildfires, floods, and landslides—posing major threats to public safety, property, shared infrastructure, and transportation corridors. In particular, compounding environmental effects from changes in precipitation patterns and rainfall extremes, more frequent wildfire, and the destruction of native vegetation coverage in highly urbanized regions make California prone to a dramatic increase in landslide hazard. As one example of these compounding effects, a major rainstorm in January 2019 led to increased landslide occurrence in areas previously burnt by the 2016 San Gabriel Complex fire and the 2014 Colby and 2009 Morris fires (Rengers et al. 2020). More recently, the California Geologic Survey and U.S. Geological Survey inventoried over 700 reported landslides in less than a month due to widespread storms in early 2023 (California Department of Conservation 2023). Globally, landslide observations suggest increasing risk in many regions due to climate change and urbanization (Ozturk et al. 2022; Cendrero et al. 2020). Studies in Central Europe (Tichavský et al. 2019) and California (Handwerger et al. 2019, 2022) have particularly emphasized the role of shifting precipitation patterns, from dry spells and droughts to extreme precipitation on landslides. Heavy rainfall events and 20-year return period amounts for daily precipitation are expected to increase in many regions (Easterling et al. 2017).

Despite developments in landslide susceptibility mapping and hazard assessment, accurate landslide forecasting is difficult, mainly due to the physical complexity of landslide triggering mechanisms and insufficient real-time measurements of surface conditions, groundwater flow, and soil/rock properties. Moreover, effects of environmental changes on landslide occurrence are nonlinear and uncertain (Gariano and Guzzetti 2022). As a result, reliable assessments of the impact of changing climate on future landslide hazard are largely lacking (Gariano and Guzzetti 2016; Crozier 2010).

In recent years, there has been increasing attention focused on connecting environmental changes and future landslide activity (Araújo et al. 2022; Tyagi et al. 2023; Hürlimann et al. 2022). General approaches include the usage of downscaled climate projections, comparison of historical landslide records with climatological or meteorological variables, and analysis of paleo-evidence, as summarized in a review by Gariano and Guzzetti (2016). Some studies rely purely on physically based models and climate projections (Guo et al. 2023; Komori et al. 2018; Alvioli et al. 2018; Lin et al. 2022), while others apply data-driven techniques (Kirschbaum et al. 2020; Shou and Yang 2015; Knevels et al. 2023; Pham et al. 2022; Park and Lee 2021; Shou and Lin 2020).

In this work, we use a novel data-driven modeling framework and a global landslide catalog to develop projections of landslide susceptibility under different climate change scenarios. We then present a detailed investigation of the temporal evolution of landslide susceptibility in California spanning 150 years. The methodology combines machine learning with statistically downscaled and bias-corrected outputs from Global Climate Models (GCMs), along with high-resolution observational datasets. After training a prediction model using historical landslide observations and meteorological datasets over the 2015–2020 period, we evaluate the capability of this model to reproduce observed landslide susceptibility for the historical baseline period. Subsequently, we derive future projections of landslide susceptibility using an ensemble of climate projections under different greenhouse gas emissions scenarios.

Methodology

Data-driven landslide model

We use XGBoost (eXtreme Gradient Boosting) (Chen and Guestrin 2016), an ensemble decision tree-based method based on boosting

techniques, as the machine learning algorithm for landslide modeling due to its superior performance in binary classification and robustness to correlated features. XGBoost has been shown to achieve a better performance in landslide susceptibility assessment compared to other machine learning techniques, e.g., random forests, artificial neural networks, and support vector machines (Cao et al. 2020). Given the inherent structure of the decision-making process, XGBoost is also resilient to correlated input features and potential extrapolation problems under future conditions (Han and Semnani 2024). This can be attributed to the fact that each decision tree performs a split based on a feature being larger or smaller than a threshold, using only one of the correlated features which leads to an optimal split. The other correlated features are disregarded in that particular split; however, may be utilized in subsequent splits. In XGBoost, weak learners based on classification and regression trees (CART) are continuously trained to fit the residuals of the previous prediction. The final prediction value of each sample is obtained by summing all the leaf scores in each tree.

The selection of appropriate landslide conditioning factors (i.e., input features of the machine learning model) is critical to the model's performance. Despite their importance, climate-related factors such as precipitation and temperature have rarely been included in data-driven landslide susceptibility models (Korup and Stolle 2014; Stanley et al. 2020). Here, we incorporated a variety of annual and seasonal precipitation metrics, along with antecedent temperature to account for climate-related influences in predicting landslides under changing climate conditions. Prior soil conditions, such as soil moisture also play a critical role in the susceptibility of slopes to failure, for instance, by affecting the amount of rainfall required to trigger such events. Due to the lack of reliable GCM outputs for soil moisture (with the resolution and measurement units consistent with historical data), we instead use antecedent rainfall and temperature data as additional model input features. To determine the number of accumulation days which adequately represent pre-existing soil conditions, we trained and evaluated the model using different antecedent day intervals (such as 10- and 30-day) and found that the antecedent 30-day interval is the most effective in predicting landslides.

Twenty-one factors were initially considered as potential inputs to the landslide model (Table 1), based on their role in providing relevant information on landslide events and pre-disposing terrain to failure, as well as the availability of data at the spatial and temporal resolutions. These considered factors fall into two main categories: (1) geoenvironmental conditions (slope, lithology, vegetation, land cover, soil type, and distance to faults) which have been shown to pre-dispose slope to failure (Corominas et al. 2014) and (2) climate-related factors (daily, seasonal and annual rainfall, as well as antecedent temperature). Using a very large number of input features in machine learning can have a negative impact on model performance due to the curse of dimensionality and potential overfitting. Therefore, we reduced the input set to the nine most important features using recursive feature elimination.

The down selection of input features was informed by an analysis of feature importance, physics insights, and Pearson correlation across variables. To reduce the input set, we first trained the XGBoost classifier using all 21 features. The XGBoost algorithm assigns three importance metrics to each feature, namely, weight, coverage, and gain. In each iteration, the least important feature is dropped according to the value of its feature importance metrics. This process is repeated recursively until the algorithm reaches the target number of features. Figure 1 shows feature importance metrics (weight, cover, and gain) for the final trained model with nine selected features.

Landslide catalogs

Data on historical landslide events are necessary to construct a comprehensive training dataset. We use NASA's Global Landslide Catalog (GLC) gridded at a 30 arcseconds daily resolution (Stanley et al. 2021), the largest publicly available global landslide inventory. It has been compiled since 2007 from various sources (Amatya et al. 2019, 2021; Geoscience Australia 2018; Benz and Stanley 2020; Secretaría de Gestión de Riesgos - Escenarios 2016; Kelkar et al. 2017; Hughes et al. 2019; Juang et al. 2019). Only landslide events triggered by rainfall are selected from this database. Since the focus of this work is landslide events which are triggered by rainfall, landslide events with unknown triggering mechanisms or those triggered by other phenomena (e.g., earthquakes, volcano, and construction) were removed from the landslide catalog. We note that a similar approach could be applied to other types of landslides using a historical landslide catalog with known (labeled) landslide type.

We use 5800 global rainfall-triggered landslide events from May 5, 2015 to April 30, 2020 with known location/time as positive samples. For negative samples, we randomly select 1.15 million non-landslide points in the same time range. The large number of negative samples (here 1.15 million points) allows the dataset to cover the wide feature space corresponding to non-landslide events.

Data for the input features for the positive and negative samples are collected from the sources listed in Table 2, forming a preliminary labeled dataset. It is noteworthy that while the case study in this work is focused on California, we choose a publicly available global dataset to obtain a larger training dataset which captures diverse climate conditions. This dataset has inherent biases and uncertainties, e.g., uncertainty in time, location, and triggering mechanism of each event (Kirschbaum and Stanley 2018). Moreover, many landslide inventories are biased toward reporting landslides in populated areas. Nevertheless, this dataset was selected in this work due to the advantages of being a large, publicly available dataset which allows us to incorporate diverse global climate conditions into the modeling process.

The dataset considered here is highly imbalanced, where the number of instances of the positive (minority) class is significantly smaller than the negative (majority) class. This is a common issue in binary classification problems due to the relative scarcity of positive samples (here, landslide events) compared to negative samples (no landslide), and can bias the learning algorithm toward the majority class. To address this problem, we use a combination of two undersampling and oversampling techniques to develop a balanced dataset by undersampling the negative data samples down to 877k and oversampling the positive data points to 877k samples. For oversampling, we use synthetic minority over-sampling technique for nominal and continuous features (SMOTE-NC), a variant of synthetic minority oversampling technique (SMOTE) (Chawla et al. 2002) which is applicable to both continuous and categorical

Table 1 Variable definitions for twenty-one initial inputs (landslide influencing factors) of the machine learning model. Nine of these features are kept in the final model (indicated by a ⋆) after recursive feature elimination

Variable name	Definition	Kept
Daily rainfall	Daily accumulated rainfall	
Normalized rainfall	Daily rainfall normalized by the 99th percentile rainfall	⋆
Antecedent rain (10-day)	Cumulative rainfall of antecedent 10 days	
Antecedent rain (30-day)	Cumulative rainfall of antecedent 30 days	⋆
Normalized antecedent rain (10-day)	Cumulative rainfall of antecedent 10 days normalized by the 99th percentile daily rainfall	
Normalized antecedent rain (30-day)	Cumulative rainfall of antecedent 30 days normalized by the 99th percentile daily rainfall	
Annual rainfall	Annual cumulative rainfall	
Wet month	Cumulative rainfall of the wettest month of the year	⋆
Dry month	Cumulative rainfall of the driest month of the year	
Wet season	Cumulative rainfall of the wettest season of the year	
Dry season	Cumulative rainfall of the driest season of the year	
Tmin (antecedent 10-day)	Averaged daily minimum temperature in the past 10 days	
Tmax (antecedent 10-day)	Averaged daily maximum temperature in the past 10 days	
Tmin (antecedent 30-day)	Averaged daily minimum temperature in the past 30 days	
Tmax (antecedent 30-day)	Averaged daily maximum temperature in the past 30 days	⋆
Distance to faults	Distance to closest faults	⋆
Slope	Maximum slope angle within each 30 arcsecond grid cell	⋆
Land cover	Land cover	⋆
Vegetation	Normalized difference vegetation index (NDVI)	
Soil type	Soil texture classification in terms of water containing capabilities	⋆
Lithology	Lithology	⋆

features. For undersampling, we have developed a new gridded hyperspace sampling approach, in which the hyperspace of input features is gridded into a specific number of intervals, and one sample from each interval is selected for inclusion in the final dataset. More details regarding the treatment of the imbalanced dataset can be found in Han and Semnani (2024).

Model validation

The balanced dataset was divided into training, testing, and validation sets, with separation ratios of 70%, 15%, and 15%, respectively. The training dataset is used for model training, and the test set is used for hyperparameter tuning. The validation dataset consists of completely unseen data and is used to calculate predictive performance metrics. The most commonly used statistical model evaluation metrics include metrics derived from the confusion matrix (Eq. 1) which includes true positive (TP), false positive (FP), true negative (TN), and false negative (FN) rates. The metrics reported here include recall (Eq. 2), specificity (Eq. 3), balanced accuracy (Eq. 4), Matthew's correlation coefficient (MCC) (Eq. 5), area under the receiver operating characteristic (AUROC), and area under the precision-recall curve (AUPRC).

$$\text{Confusion Matrix} = \begin{bmatrix} TN & FN \\ FP & TP \end{bmatrix} \tag{1}$$

$$\text{Recall} = \frac{TP}{TP + FN} \tag{2}$$

$$\text{Specificity} = \frac{TN}{TN + FP} \tag{3}$$

$$\text{Balanced Accuracy} = \frac{1}{2} \times \left(\frac{TP}{TP + FN} + \frac{TN}{TN + FP} \right) \tag{4}$$

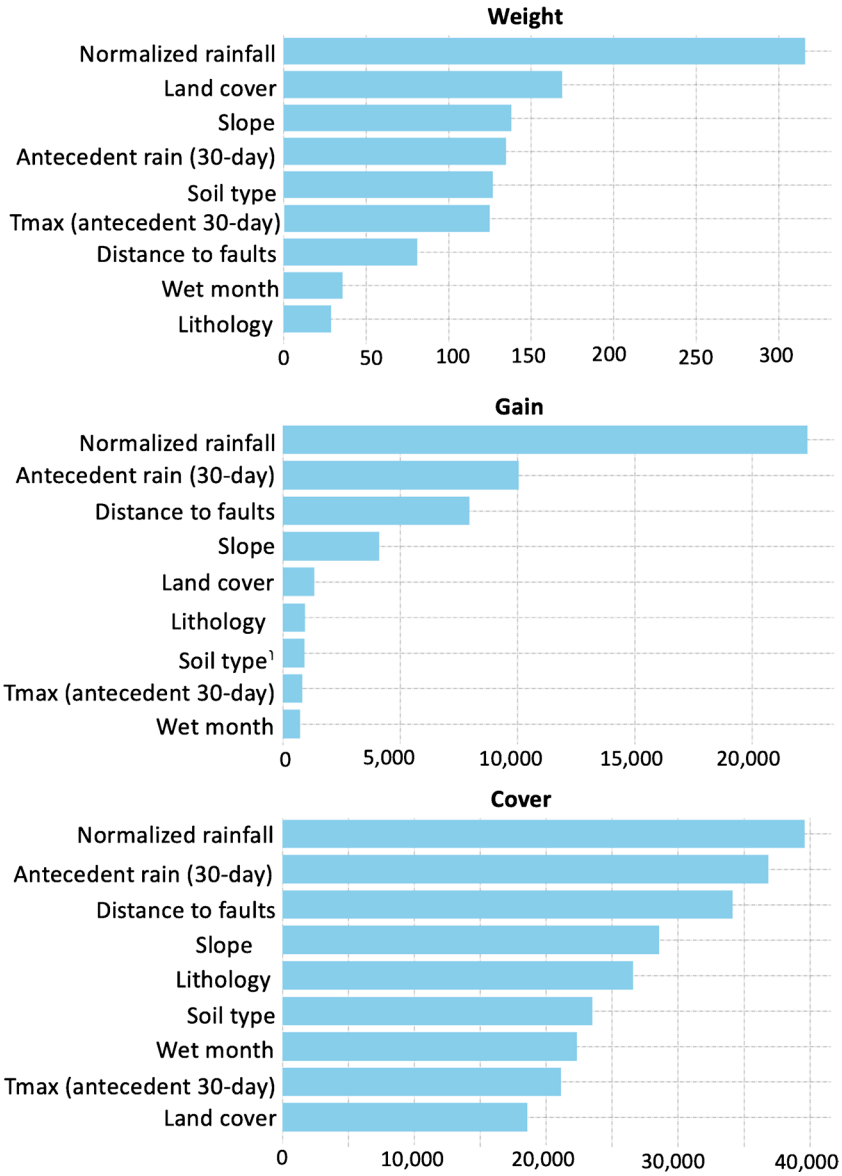

Fig. 1 Feature importance (cover, gain, and weight) given by the model trained with the 9 selected features

$$\mathrm{MCC} = \frac{TP \times TN - FP \times FN}{\sqrt{(TP + FP) \times (TP + FN) \times (TN + FP) \times (TN + FN)}} \quad (5)$$

The above metrics are calculated on the validation dataset to evaluate the model performance, as shown in Table 3. Since we are particularly interested in the model's capability to predict landslide events, we also calculate the Recall and Specificity on all "real" validation samples (i.e., the samples that are not generated/removed during undersampling and oversampling process), yielding Recall = 0.91 and Specificity = 0.99. The positive samples in this set consist of real landslide events from the landslide catalog which are completely unseen by the model during training/hyper-parameter tuning, demonstrating the satisfactory performance of the model in the prediction of landslide events. Finally, the generated California landslide susceptibility maps (see the "Landslide susceptibility mapping" section) are compared with historical landslide inventories, as shown in Fig. 2c.

Landslide susceptibility mapping

We develop a data-driven landslide model using XGBoost as the machine learning algorithm, as described in the "Data-driven landslide model" section. The model is trained on historical data and produces a daily estimate of landslide probability at a given location based on local site parameters and historical/projected meteorological conditions (daily rainfall, antecedent rainfall and temperature, and cumulative rainfall of the wettest month of the year). We use the trained model to generate landslide susceptibility maps of California with a spatial resolution of 0.01 degree (about

Table 2 Dataset information

Dataset	Spatial resolution	Temporal resolution	Unit
Slope (de Ferranti 2015)	30 arcseconds	–	Degree
Distance to faults	30 arcseconds	–	Km
(Styron and Pagani 2020)			
Soil texture (Webb et al. 2000)	1/30 degree	–	–
Lithology	0.5 degree	–	–
(Hartmann and Moosdorf 2012)			
Land cover	1 arcsecond	–	–
(European Space Agency 2017)			
Precipitation (observations)	0.1 degree	Daily	Millimeter
(Huffman et al. 2019)			
Precipitation (climate projections)	0.0625 degree	Daily	$Kg/m^2/s$
(Pierce et al. 2018)			
Temperature (observations)	0.5 degree	Daily	Celsius degree
(NOAA PSL 2021)			
Temperature (climate projections)	0.0625 degree	Daily	Kelvin
(Pierce et al. 2018)			

Table 3 Model performance metrics of the final trained model calculated on the validation dataset

Info/metric	
Recall	0.952
Specificity	0.965
Balanced accuracy	0.959
MCC	0.917
AUROC	0.99
AUPRC	0.99

1 km). The specific resolution is chosen based on the available resolution of the input features and downscaled climate variables. For each grid cell, the landslide influencing factors are evaluated and used as input to the model to obtain daily predictions of landslide probability for the given cell.

To produce susceptibility maps, we first define an aggregate susceptibility index in each grid cell. A collection of probabilities over multiple days in a year (here 30 days) are obtained and averaged to determine the susceptibility index of each grid cell to reduce the effects of machine learning model uncertainty and random daily variability in dynamic precipitation and temperature data. The susceptibility index of each grid cell is calculated by averaging the predicted probabilities of 30 days in a given year with the highest probabilities and then averaging yearly values in a given time period of interest (e.g., 1990–2020).

The resulting susceptibility indices are then used to classify grid cells into one of five susceptibility categories (from "very low" to "very high" susceptibility). Different zoning techniques have been used in the literature to classify landslide maps into categories, for example, geometric interval method (Wang et al. 2023), quantile classification, natural breaks (Jenks) method, equal interval classification, and standard deviation-based classification (Ayalew et al. 2004). In this work, after obtaining the continuous susceptibility maps, we categorize the susceptibility values into categories using equal intervals as follows: 0–0.2 (very low); 0.2–0.4 (low); 0.4–0.6 (medium); 0.6–0.8 (high); and 0.8–1 (very high).

As explained in the "Model validation" section, the landslide prediction model is quantitatively validated using a validation dataset composed of 15% of the original catalog, demonstrating excellent performance metrics (Table 3). As an additional test, the model is used to produce a 30-year susceptibility map for California over the 1990–2020 period (Fig. 2a) using climatological data derived from CNRM-CM5 simulations as inputs. The histogram in Fig. 2c shows the number of California historically observed rainfall-triggered landslide events from the dataset which fall in each susceptibility category, obtained from the historical landslide susceptibility map of 1990–2020 time period. As expected, most of the landslide events fall in areas with very high landslide susceptibility, and the number of landslides in

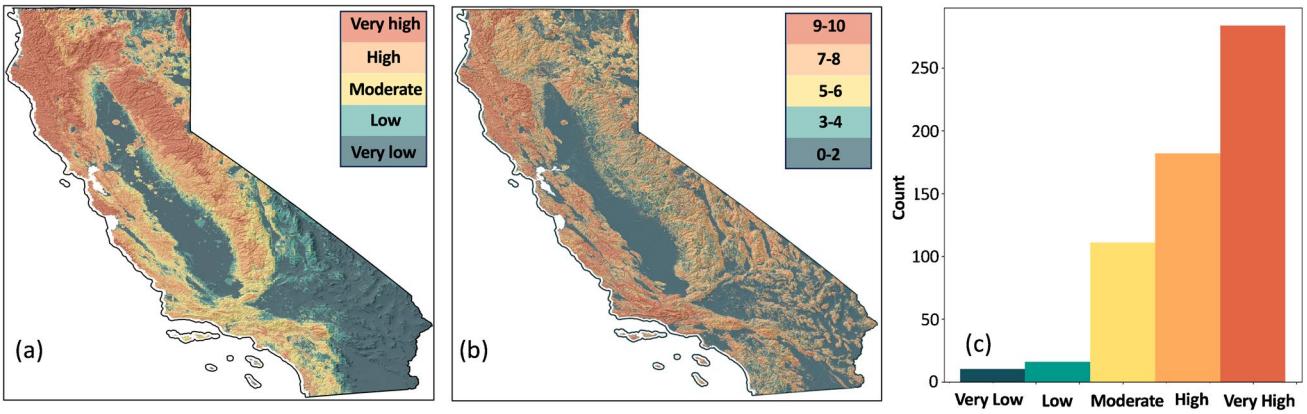

Fig. 2 **a** Categorized landslide susceptibility map for 1990–2020 (using CNRM-CM5 simulations as inputs), compared with **b** the California Geological Survey (CGS) deep-seated landslide susceptibility map. The CGS map is modified from Wills et al. (2011) with permission from the California Geological Survey, where landslide susceptibility classes (0 to 10, low to high) are grouped as shown. **c** Histogram of historical landslides located in each classification region in the map (**a**)

each category decreases with the degree of susceptibility. It is observed that the model reliably identifies higher-susceptibility regions consistent with the historical record.

For comparison, a deep-seated landslide susceptibility map developed by California Geological Survey (CGS) is shown in Fig. 2b. We note that the CGS map is determined based on slope and lithological strength alone, and does not include any climate information like precipitation metrics. The CGS map is developed for deep-seated landslides, while the present model accounts for all landslide types contained in the training catalog. The regions identified as "very high" to "high" susceptibility in our model are generally predisposed to deep-seated landslides. Overall, the model results are spatially consistent with the CGS map. Major differences are observed, however, in the inland desert region to the southeast of the state. While this region includes areas with large slopes and/or weak rocks, the lack of heavy precipitation results in very low susceptibility to landslides.

Climate projections

California's topography includes extensive mountainous regions as well as areas of flatter terrain. Its climate is mainly Mediterranean, marked by a dry and a wet season, modulated by year-to-year variability and extreme weather events. Its temperatures are milder along the coast and with greater seasonal contrast inland. Due to its higher latitude and elevation, the northern part of California receives more rainfall through winter storms and atmospheric rivers and possesses some of the rainiest areas and steep slopes. Estimating the implications of climate change in such a climatically and topographically complex region is challenging.

In this work, we leverage the Coupled Model Intercomparison Project Phase 5 (CMIP5) daily climate projections. Since most GCMs have a spatial resolution of about 100 km, which is too coarse to capture California's diverse topography and complex climate, we need to rely instead on statistically downscaled and bias-corrected outputs (e.g., temperature, precipitation, humidity, or wind speed), to better account for topographical effects. To reach this goal, the California Department of Water Resources (DWR) Climate Change Technical Advisory Group (Lynn et al. 2015) evaluated thirty-two CMIP5 GCMs and selected a subset of ten models which have the best performance for simulating the historical climate of California. Climate projections from these ten GCMs were bias-corrected and downscaled to a spatial resolution of 0.0625 degrees (about 6 km) using Localized Constructed Analogs (LOCA). Compared to previous statistical downscaling methods applied to refine California's climate, LOCA has been recognized to better represent extreme weather conditions (such as heatwave or extreme precipitation events) (Pierce et al. 2018, 2013). The publicly available dataset provides daily precipitation and temperature data over California, from 1950 to 2005 for the historical period, and projections from 2006 to 2100 (Pierce et al. 2018). This dataset includes a total of two different emission scenarios, namely, the Representative Concentration Pathways 4.5 (RCP4.5) representing a medium emission scenario with stabilization, and RCP8.5 representing a high baseline scenario in which the emissions continue to increase through this century (Van Vuuren et al. 2011). In support of California's Fourth Climate Change Assessment sponsored by the California Energy Commission, Pierce et al. (2018) further assessed the downscaled outputs from these ten California GCMs. The authors recommended a narrower selection of four climate models based on their ability to reliably simulate California's historical climate, while still capturing similar inter-model variability seen in larger ensembles and providing a range of plausible climate projections. These four are HadGEM2-ES (a "warm/dry" model), CanESM2 (an "average" model), CNRM-CM5 (a "cool/wet" model), and MIROC5 (most unlike the first three). To reduce the computational costs associated with conducting this study at high resolution (1 km), we utilize these four climate models which are able the capture inter-model variability across temperature, precipitation, and extreme rainfall projections (Pierce et al. 2018). To illustrate this, we compare daily and antecedent rainfall trends obtained from the four-model ensemble with the ensemble of 10 models selected by DWR, as explained below. While larger ensembles are preferable, we observe that the

four selected models strike a balance between capturing inter-model variability and modeling practicality.

Trend analyses of precipitation are commonly used in climate change studies (Mudelsee 2019). Here, we obtain daily rainfall trend maps shown in Figs. 3 and 4 to compare different climate models. The procedure for obtaining these daily rainfall trend maps is as follows. For any given grid cell, 30 days with the highest landslide susceptibility in any given year are determined. For these 30 days, the daily rainfall values are calculated and averaged. These values are plotted over the years from 1950 to 2100 and a regression line is fit to the data to obtain the trend for any given grid cell. Results are plotted for all grid cells to form the trend maps.

Figure 3 shows the daily precipitation trends over 1950–2100 from the ten California GCMs, including the four GCMs selected by Pierce et al. (2018), as marked. There is significant inter-model variability, with CanESM2, CNRM-CM5, and CESM1-BGC showing the largest increase in precipitation trend. Figure 4 shows the 1950–2100 trend maps of daily rainfall and antecedent 30-day rainfall obtained from averaging the ten models chosen by DWR and the four down-selected models, along with their respective inter-model variability map. For both indices, the average trend maps are not very sensitive to the number of climate models employed. In the RCP4.5 case, both the average and variability maps derived from the ten models are closely captured by the four models. In RCP8.5, there is a slightly larger average and variability in the ten-model case compared to the four-model case. Overall, these results corroborate the findings of Pierce et al. (2018) showing that the selected four climate models are sufficiently representative of climate variability in California. We adopt these four models to investigate the effects of climate change conditions on landslide susceptibility.

According to Pierce et al. (2018) and based on the results of ten models, the average annual temperature over California will increase through the century in both RCP scenarios, with a clear separation occurring around 2050. The precipitation projections show that,

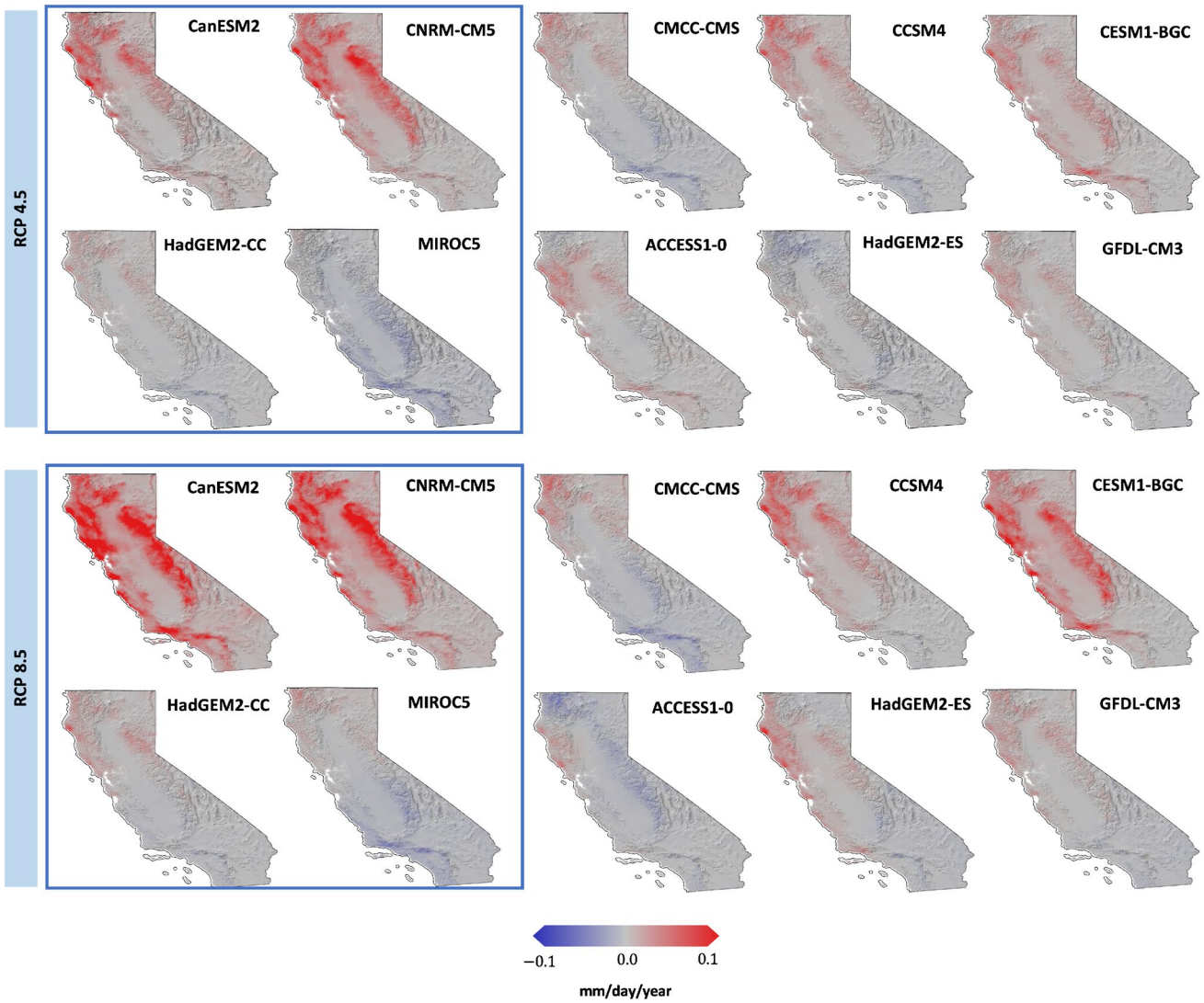

Fig. 3 Daily rainfall trend obtained from 10 climate models under RCP4.5 and RCP8.5 scenarios over 1950–2100. The models used in the landslide study are marked

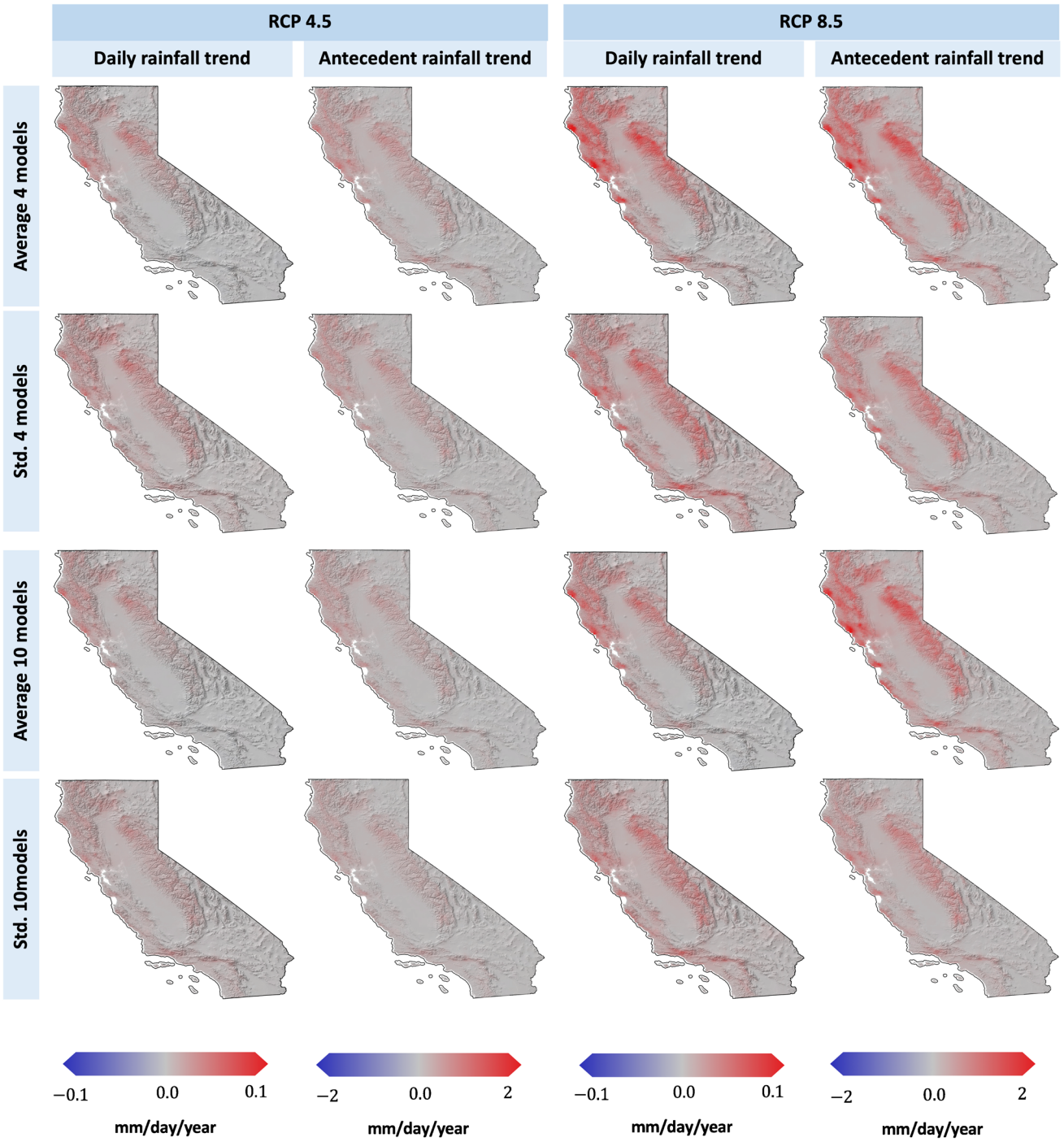

Fig. 4 Daily rainfall and antecedent 30-day rainfall trends obtained from the average of 4 and 10 climate models under RCP4.5 and RCP8.5 scenarios over 1950–2100. Standard deviations across models in each case are also shown

despite relatively small mean changes, there is a projected increase in year-to-year variability due to fewer rainy days but more intense wet days. A seasonal change in precipitation is also expected with increasingly wetter winters and drier springs. Through this century, the wettest day is projected to increase, with increases of 20 – 35% in the coastal ranges under RCP8.5 (Pierce et al. 2018). Other studies indicate that both the magnitude and frequency of extreme rainfall events will increase in response to climate change (Gründemann et al. 2022; Prein et al. 2017). Overall, these seasonal changes, their variations across California, and the more frequent extreme precipitation events are expected to have important implications for susceptibility to landslides.

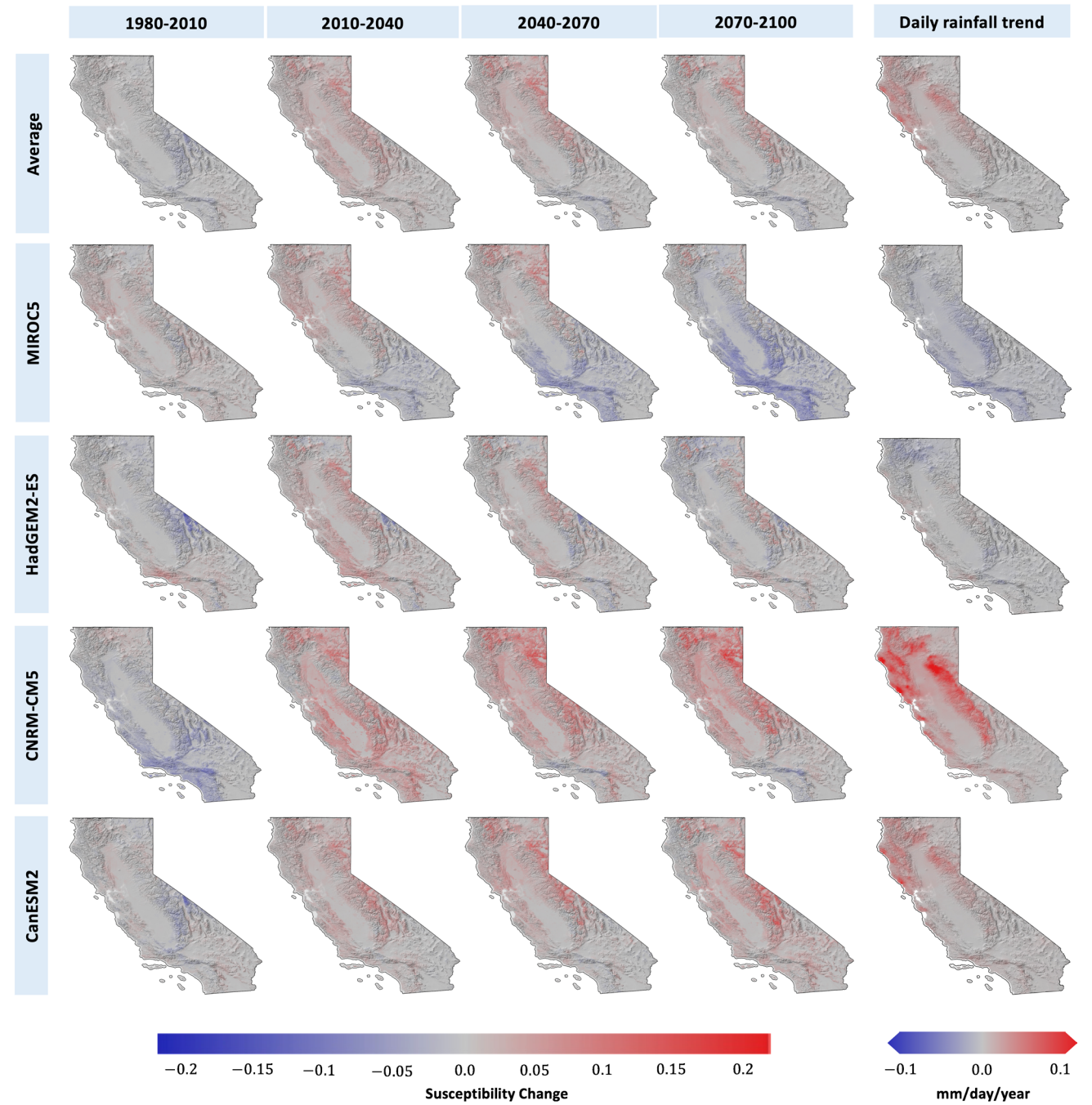

Fig. 5 Landslide susceptibility changes compared to 1950–1980 obtained from four climate models under RCP4.5, along with the daily rainfall trend maps for 1950–2100 under RCP4.5

Results

Landslide susceptibility in a changing climate

After validating the performance of the model using historical data, we derive landslide susceptibility maps in response to projected climate. For this purpose, we take climate input features from the downscaled and bias-corrected daily precipitation and temperature data obtained from the selected climate models and the two RCP emission scenarios (see the "Climate projections" section), and use them to predict daily landslide probabilities for all locations across the state and calculate the susceptibility indices. Four climate models are used for this purpose: HadGEM2-ES (warm/dry model), CanESM2 (average model), CNRM-CM5 (cool/wet model), and MIROC5 (most unlike the first three). To obtain susceptibility, for each grid cell, we select 30 days with the highest landslide probability in any given year and average the results over 30-year time periods. We adopt a non-overlapping 30-year sliding window approach to capture slowly evolving changes in climate

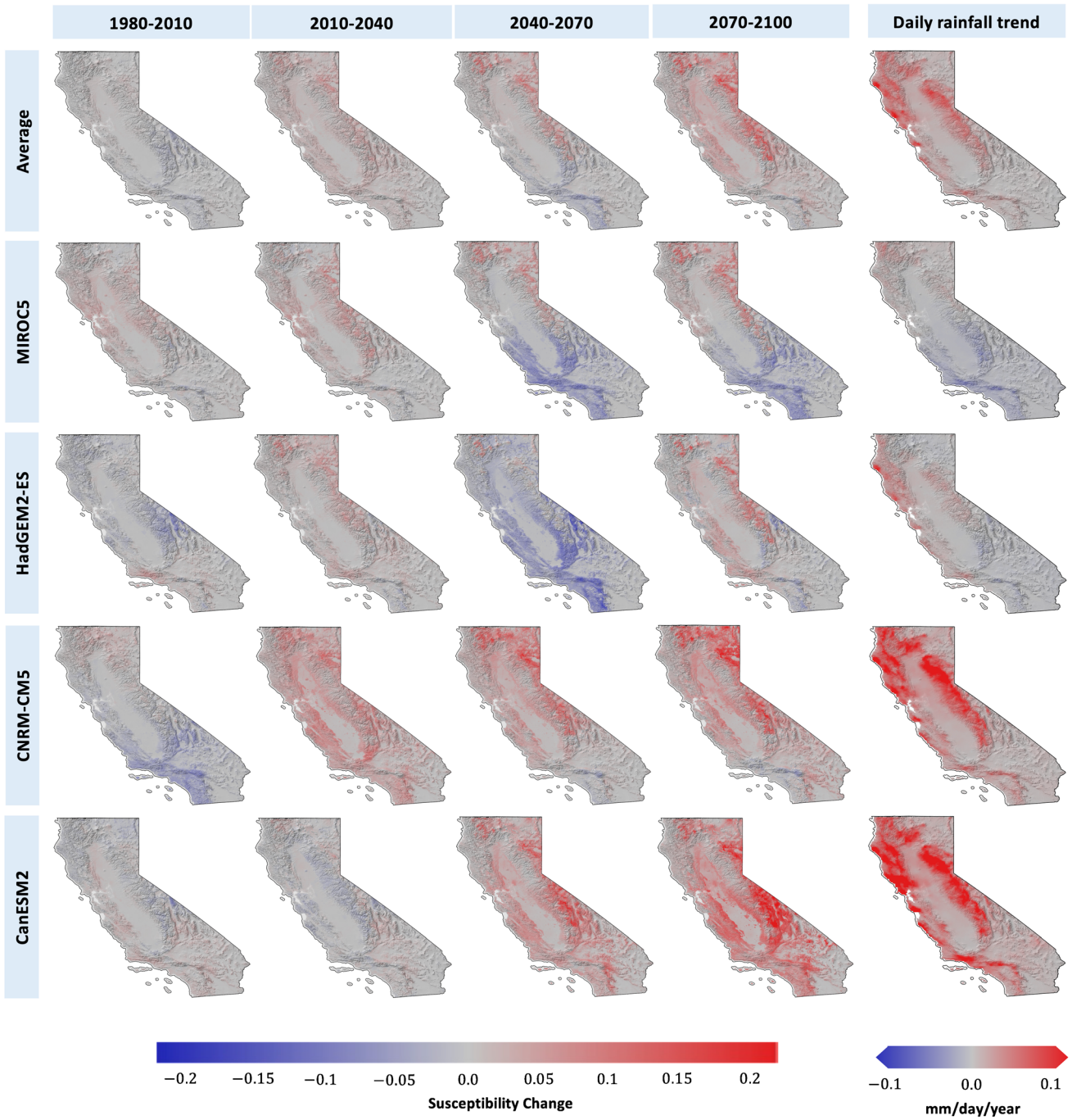

Fig. 6 Landslide susceptibility changes relative to the 1950–1980 reference period obtained from four climate models under RCP8.5, along with the daily rainfall trend maps over the entire 1950–2100 period under RCP8.5

conditions (rather than changes induced by year-to-year internal climate variability), which is a standard method in climate research (e.g., Hulme et al. 1999). We have selected 5 non-overlapping sliding time windows in this study: 1950–1980, 1980–2010, 2010–2040, 2040–2070, and 2070–2100. We select the period of 1950–1980 as a reference to show evolving susceptibility changes. This choice of baseline period effectively optimizes the use of the downscaled datasets starting from 1950. Although we did not specifically test the sensitivity of our susceptibility results to variations in the baseline period, Pierce et al. (2018) investigated the sensitivity of temperature and precipitation changes to the baseline period (1976–2005 versus 1961–1990) and found about +0.3 °C difference in daily minimum and maximum temperatures (i.e., aligning reasonably with climate change expectation), and very small difference in precipitation. Based on these results, we believe that the baseline selection would not fundamentally alter our results or conclusions, nor

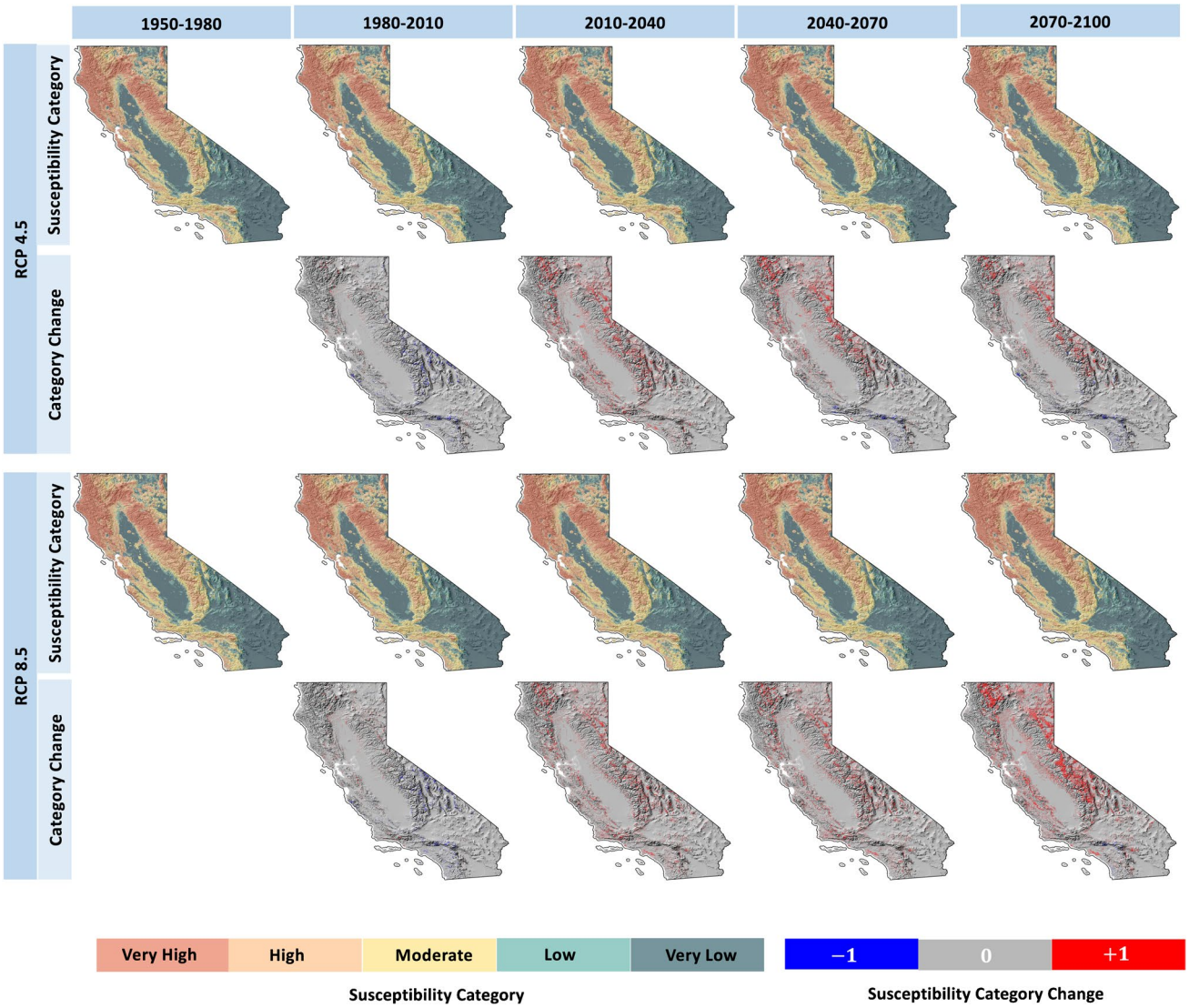

Fig. 7 Categorized landslide susceptibility maps over 30-year time periods and changes in landslide susceptibility categories compared to the 1950–1980 reference period obtained from the average of four climate models under RCP4.5 and RCP8.5

impact the interpretation of the different 30-year sliding windows, analyzed side by side.

Figures 5 and 6 show evolving susceptibility changes at 1 km resolution under RCP4.5 and RCP8.5, respectively, for different time frames relative to the reference period of 1950–1980. The continuous susceptibility values produced by the model, ranging between 0 and 1, are used to compute susceptibility changes from the baseline period. Increasing values indicate increasing susceptibility. Results are shown for the individual climate models and for the multi-model average (MMA), along with trend maps of extreme daily rainfall (the most important input feature) calculated between 1950 and 2100 for reference. Each individual model produces similar spatial landslide susceptibility and rainfall trend patterns under RCP4.5 and RCP8.5 emission scenarios, but with higher intensity in the RCP8.5 case. The maps show an increase in landslide susceptibility using the CNRM-CM5 and CanESM2 models, particularly in the Sierra Nevada, North Coast, and Central Coast regions. Landslide susceptibility estimates using the HadGEM2-ES and the MIROC5 models show a positive trend in some regions, and a negative trend in other areas. Overall, susceptibility trends are strongly linked to the precipitation trends seen in each GCM, as directly observed from Figs. 5 and 6.

Figure 7 shows the same results, but employing the discrete classification system with five susceptibility categories. These categorical MMA susceptibility maps show very high and high susceptibility in the Sierra Nevada and the coastal ranges. To better identify the areas subject to a change in susceptibility category as a result of climate change, we select the susceptibility map corresponding the time period of 1950–1980 as a baseline. Subsequently, we obtain the category difference maps by subtracting the baseline map from maps corresponding to later time

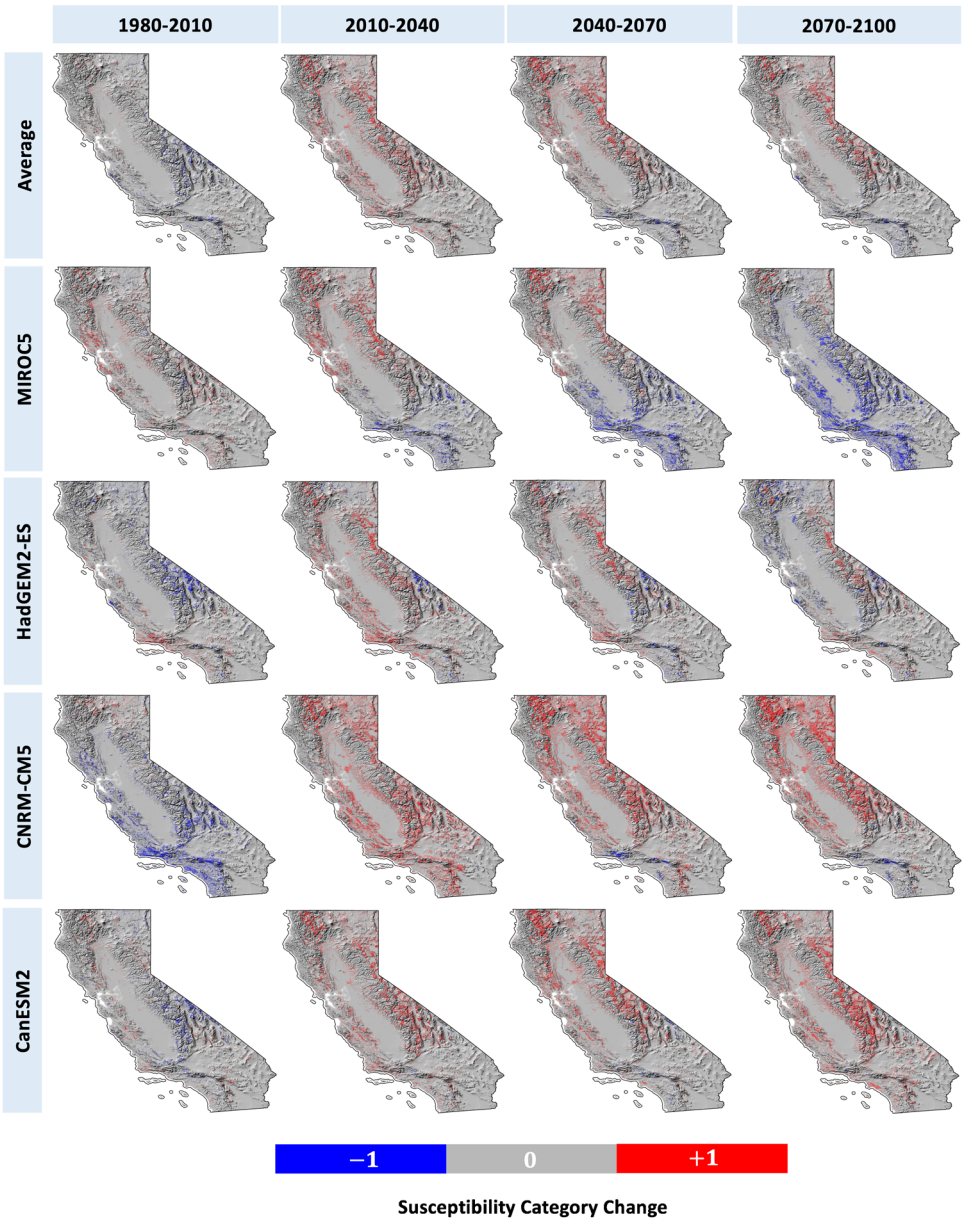

Fig. 8 Changes in landslide susceptibility categories compared to the reference time period of 1950–1980 obtained from 4 climate models under RCP4.5

periods (Fig. 7). Figures 8 and 9 show the mapped changes in susceptibility categories for each of the four individual climate models. The category difference maps in Figs. 7, 8, and 9 provide a visual representation of areas in which landslide susceptibility will increase (+1) or decrease (−1) by one category. Areas in which no change in the susceptibility category is observed are shown as 0. The difference MMA maps in Fig. 7 indicate that the susceptibility of a significant portion of the state is increasing by one level through the end of this century, according to the average of climate models. Difference maps of the individual models in Figs. 8 and 9 show that some models (MIROC5 and HadGEM2-ES) predict one level of reduction in the landslide susceptibility level in the southern half of California, while other parts show one level of increase. Using CNRM-CM5 and CanESM2 models, predicted changes primarily indicate one level of increase in susceptibility category rather than decrease.

Figures 5 and 6 indicate that the susceptibility to landslides can increase by approximately 15% and 20% in some regions, as simulated by the CNRM-CM5 model under the RCP4.5 and RCP8.5 emission scenarios, respectively. In addition, the increase in susceptibility becomes more pronounced in the mid-century (2040–2070) and in the late century (2070–2100) in response to the increasing forcing. Driven by its simulated drying climate conditions, the results obtained from the HadGEM2-ES (warm-dry) model show a smaller increase in landslide susceptibility compared to CNRM-CM5 (cool-wet) model or the CanESM2 (average) model. Under the

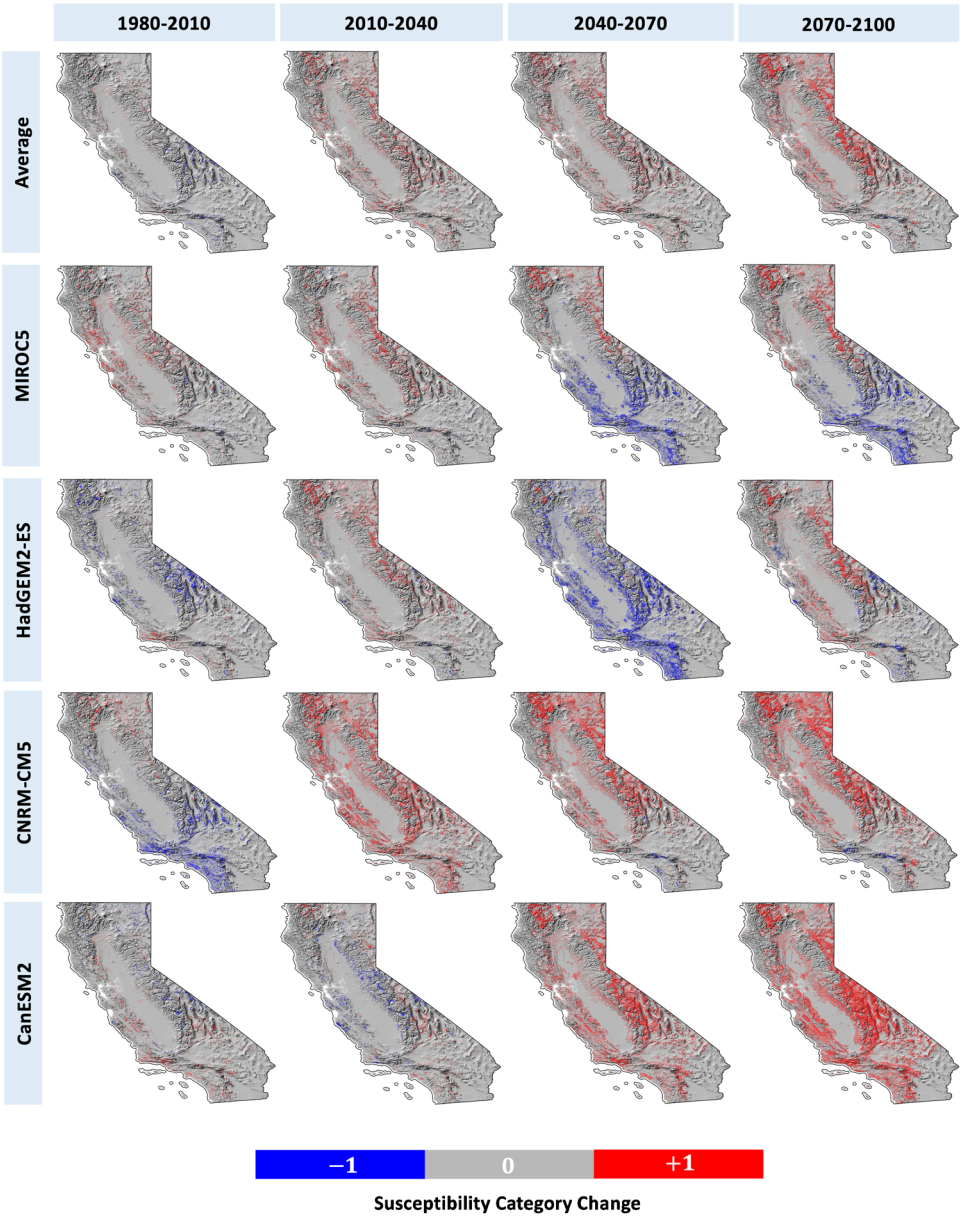

Fig. 9 Changes in landslide susceptibility categories compared to the reference time period of 1950–1980 obtained from 4 climate models under RCP8.5

RCP8.5 scenario, landslide susceptibility simulated by HadGEM2-ES increases up to 10% (Fig. 6, time period 2070–2100), but this occurs in a much smaller portion of the state compared to CNRM-CM5, while landslide susceptibility decreases over a significant portion of the state.

Under the RCP8.5 scenario, the variability across the four models is large. As observed in Figs. 8 and 9, CNRM-CM5 and CanESM2 models both indicate that a large portion of California will increase one category in susceptibility (e.g., from moderate to high and from high to very high). The HadGEM2-ES model also indicates an increase in susceptibility category in 2070–2100, but only after a period of decrease in landslide susceptibility (2040–2070). In contrast, MIROC5 indicates a slow but steady increase in susceptibility over the northern part of the state but a steady decrease in its southern part. Most of these results are directly driven by the projected changes in extreme daily rainfall and antecedent rainfall, themselves subject to a large variability across decades and across models. These interdecadal fluctuations could be a simple manifestation of internal climate variability, or result from model uncertainties in projecting rainfall changes in response to human activities. In analyzing the sign agreement of the changes in mean precipitation averaged over the winter season, Neelin et al. (2013) showed that 90% of all CMIP5 models display an increase in precipitation north of approximately 40° N, and 80% agree on the reduction of the precipitation farther southward, over much of the subtropical

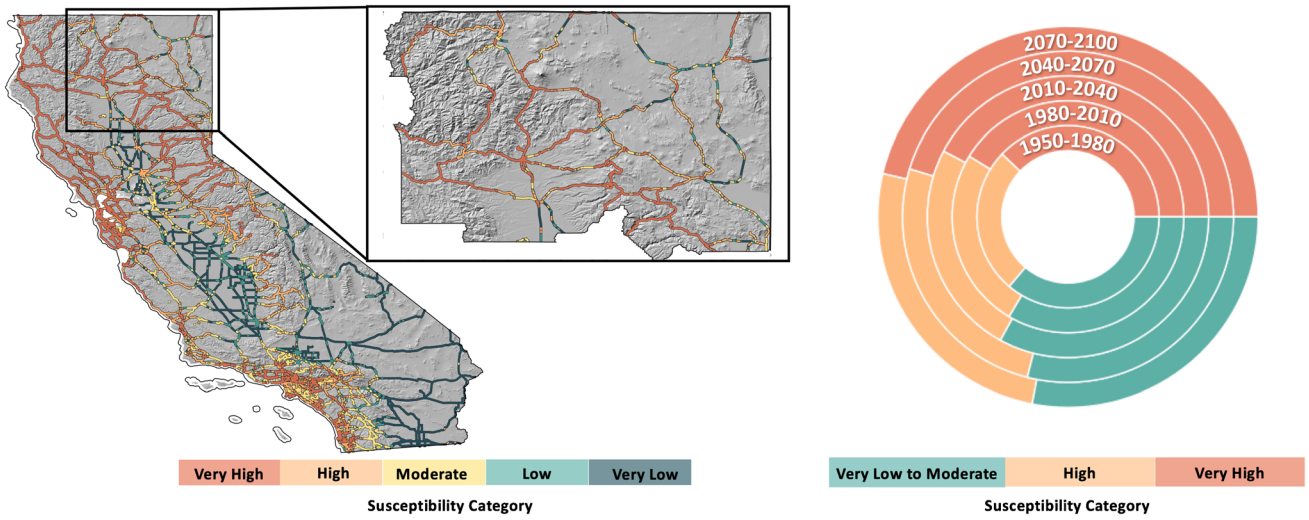

Fig. 10 Left: Landslide susceptibility category maps of California roadways corresponding to the average of all four climate models under RCP8.5 in 2070–2100. The inset shows the region corresponding to District 2. Right: Time evolution of percentage roadways of California District 2 corresponding to susceptibility categories of very low to moderate, high, and very high obtained from four climate models under RCP4.5 and RCP8.5

regions, with some uncertainties on the location of the boundary between two features.

Despite a visible and significant inter-decadal and inter-model variability, the MMA results depict an underlying forced component indicating a slowly evolving but clear increase in landslide susceptibility, especially in California's northern parts and in the slopes of the Sierra Nevada. Results of Figs. 7, 8, and 9 also highlight that changes in landslide susceptibility vary from one location to another, and it is not advisable to average changes across the entire state.

Impact on roadways

We investigate the vulnerability of California's roadway system by overlaying the highway network on landslide susceptibility maps obtained from our model for all time periods. We use the 2019 roadway dataset from the U.S. Census Bureau, Department of Commerce (2019), which includes primary and secondary roads. To obtain roadway susceptibility maps, the roadway network is overlaid on the susceptibility maps, and each roadway segment is labeled according to the susceptibility of the grid cell in which it is located. For example, Fig. 10(left) shows this process for the MMA under the RCP8.5 emission scenario in 2070–2100 time period. We use the landslide susceptibility maps developed under different climate scenarios to identify California's roadways located in the regions with increased and/or significant landslide potential. These maps are compared with the current susceptibility maps to provide crucial information about potential changes in vulnerability.

Figure 10 shows the vulnerability of the roadway system based on the five-category classification, using the MMA and the RCP8.5 scenario during the 2070–2100 period. Roadway segments with vulnerability of very high are identified, including regions around the northern coast ranges, San Francisco, Los Angeles, San Diego, and the east side of the Central Valley. We also study the change in roadway mileage and state area in each susceptibility category. For Department of Transportation District 2, Fig. 10(right) shows an increasing trend for the roadways with high and very high susceptibility in 2070–2100 under MMA RCP8.5. Figure S6 shows that the portion of very high and high susceptibility areas and roadways generally increase with time according to CNRM-CM5, CanESM2, and the MMA, while HadGEM2-ES and MIROC5 show greater temporal fluctuations.

Discussion

Complex outcomes of global climate change have affected precipitation patterns and have led to increased rainfall intensity and wildfires in various areas, which can lead to increased risk of landslides. To date, a significant gap exists in our quantitative understanding of the connections between evolving climate and landslide susceptibility. To address this gap, we have developed a susceptibility assessment framework and applied it to estimate the future vulnerability of California districts and transportation infrastructure under different climate scenarios, with the following key conclusions.

The ensemble of models indicates an increase in landslide susceptibility through the 2100 time frame, in regions with a historical susceptibility classified as moderate to very high. The results, however, show that the conclusions regarding the changes in landslide susceptibility and roadway segments with high and very high vulnerability are sensitive to the choice of the climate model and emission scenario. A range of emissions scenarios therefore needs to be considered. The CNRM-CM5 (cool/wet) climate model shows a continuing increase in susceptibility through 2100, while the HadGEM2-ES (warm/dry) model shows a decreasing trend in susceptibility in 2040–2070 time period followed by a subsequent increase in 2070–2100 (Fig. 6). This result is expected because the cool-wet model generally predicts larger precipitations compared to the warm-dry model (Fig. 3). Although the spatio-temporal variations in landslide susceptibility are sensitive to climate model

Fig. 11 Time evolution of percentage area and roadways of California District 2 corresponding to each susceptibility categories of very low to moderate, high, and very high obtained from 4 climate models under RCP4.5 and RCP8.5

uncertainties in predicting extreme rainfall, the direst impacts are largely circumvented in lower emission scenarios.

The results of this study indicate an increase of up to approximately 10% in state-wide landslide susceptibility (according to the CNRM-CM5 and CanESM2 models) by 2070 under the RCP4.5 mild emission scenario (Fig. 5), and by 2040 under the RCP8.5 high emission scenario (Fig. 6). Using the HadGEM2-ES model, no increase in the state-wide percentage of area and roadways with very high susceptibility is projected. However, there are various locations with changes of ±15% in susceptibility by 2100 under both emission scenarios. These observations highlight the importance of considering geospatial variations in landslide susceptibility in addition to the total changes in the state, as large-scale spatial averaging may mask localized effects.

Roadway segments with very high vulnerability increase with time. The results obtained for time evolution of percentage area and lengths of roadway segments with the vulnerability of very high within California show variations from district to district, with an overall increase in vulnerability expected in some districts (e.g., District 2, see Fig. 11).

The impact of climate change on landslides has not been addressed in previous California's Climate Change Assessments. The results of this study can inform ongoing climate change impact assessment efforts, e.g., California's Fifth Climate Change Assessment initiative which investigates the climate-related vulnerability in California. Moreover, this study demonstrates a methodology which can be beneficial for prioritizing and guiding investments to mitigate the effects of climate change on the vulnerability of roadways and transportation system.

Limitations and future work

The focus of this work is landslide events which are triggered by rainfall. Therefore, landslide events with unknown triggering mechanisms or those triggered by other phenomena (e.g., earthquakes,

volcano, and construction) were removed from the landslide dataset. Nevertheless, a similar technique can be applied to other types of landslides. In addition, due to lack of reliable downscaled climate projection data on snow mass and snowmelt, landslides triggered by snowmelt were also excluded from the dataset. Investigation of more complex triggering mechanisms (such as snowmelt) on landslide susceptibility is left for future work. Prioritizing research on the development of downscaled and bias-corrected climate projection data for snow mass and snowmelt would enhance our ability to assess landslide susceptibility triggered by snowmelt events. Moreover, the present work focuses on landslide types including debris flow and deep-seated landslides. Other landslide types (e.g., rockfall, topple) or unknown types were removed from the dataset to improve model robustness.

As discussed in the "Landslide catalogs" section, in general, scarcity of publicly available landslide data, uncertainty in locations, time and triggering mechanisms of landslide events, and bias in the datasets are perennial issues in landslide susceptibility assessment efforts. Despite the inherent biases and uncertainties reported in NASA GLC dataset (Kirschbaum and Stanley 2018), this dataset has been adopted in this study since it is a large, publicly available dataset which allows us to incorporate diverse global climate conditions into the modeling process. Considering the critical role of landslide data on model quality, improvement of landslide data quality is an important avenue for future work (Mirus et al. 2020).

We also note the importance of variability in climate model predictions. The four climate models used in this work were selected by Pierce et al. (2018) to strike a balance between capturing similar inter-model variability seen in larger ensembles and computational costs. Nevertheless, using a larger ensemble of climate models in future work would better inform the forced and unforced components governing the future changes in landslides, and would help to more accurately assess the role of climate model uncertainty on landslide susceptibility.

The pixel resolution of 1 km was selected in this work due to the large study area and limited resolution of the precipitation datasets. In high risk regions, more detailed site characterization, risk assessment, and resilience planning is required. An example includes identifying regions/roadways of high/increased susceptibility for mapping at a higher resolution, e.g., at the slope scale.

This work provides a novel data-driven method for quantitative assessment of the impacts of climate change on landslide susceptibility through this century, and identifying regions and roadways with high and/or increased susceptibility. Despite the aforementioned limitations, the use of machine learning and projections from global climate models shows promising results for landslide susceptibility assessment. The results of this work can provide a guide to prioritize more detailed risk mitigation studies and infrastructure investment decisions.

Acknowledgements

This work used Expanse at the San Diego Supercomputer Center through allocation CIV23005 from the Advanced Cyberinfrastructure Coordination Ecosystem: Services & Support (ACCESS) program (Boerner et al. 2023), which is supported by U.S. National Science Foundation grants No. 2138259, 2138286, 2138307, 2137603, and 2138296. The authors wish to thank colleagues at the California Geological Survey for providing map data presented in Figure 2.

Funding

Funding for this work was provided by NASA under Grant No. 80NSSC22K0139. Portions of this work were performed under the auspices of the U.S. Department of Energy by Lawrence Livermore National Laboratory under contract DE-AC52-07-NA2734.

Data availability

The data generated during the course of this study are available from the corresponding author upon reasonable request.

Declarations

Conflict of interest The authors declare no competing interests.

References

Amatya P, Kirschbaum D, Stanley T (2019) Use of very high-resolution optical data for landslide mapping and susceptibility analysis along the Karnali highway. Nepal. Remote Sens 11(19):2284. https://doi.org/10.3390/rs11192284

Amatya P, Kirschbaum D, Stanley T, Tanyas H (2021) Landslide mapping using object-based image analysis and open source tools. Eng Geol 282:106000. https://doi.org/10.1016/j.enggeo.2021.106000

Alvioli M, Melillo M, Guzzetti F, Rossi M, Palazzi E, Hardenberg J, Brunetti MT, Peruccacci S (2018) Implications of climate change on landslide hazard in Central Italy. Sci Total Environ 630:1528–1543. https://doi.org/10.1016/j.scitotenv.2018.02.315

Araújo JR, Ramos AM, Soares PM, Melo R, Oliveira SC, Trigo RM (2022) Impact of extreme rainfall events on landslide activity in Portugal under climate change scenarios. Landslides 19(10):2279–2293

Ayalew L, Yamagishi H, Ugawa N (2004) Landslide susceptibility mapping using GIS-based weighted linear combination, the case in Tsugawa area of Agano River, Niigata Prefecture, Japan. Landslides 1:73–81

Boerner TJ, Deems S, Furlani TR, Knuth SL, Towns J (2023) ACCESS: advancing innovation: NSF's advanced cyberinfrastructure coordination ecosystem: services & support. In: Practice and Experience in Advanced Research Computing, pp 173–176

Benz G, Stanley T (2020) Pokot landslide inventory. NASA, Greenbelt, Maryland, USA

California Department of Conservation (2023): 2023 California Landslide Response

Chawla NV, Bowyer KW, Hall LO, Kegelmeyer WP (2022) SMOTE: synthetic minority over-sampling technique. J Artif Intell Res 16:321–357. https://doi.org/10.1613/jair.953
Cendrero A, Forte L.M, Remondo J, Cuesta-Albertos JA (2020) Anthropocene geomorphic change. Climate or human activities? Earth's Futur 8(5):1–13. https://doi.org/10.1029/2019EF001305
Chen T, Guestrin C (2016) XGBoost: a scalable tree boosting system. In: Proceedings of the 22nd ACM SIGKDD International Conference on Knowledge Discovery and Data Mining,pp 785–794
Crozier MJ (2010) Deciphering the effect of climate change on landslide activity: a review. Geomorphol 124(3–4):260–267. https://doi.org/10.1016/j.geomorph.2010.04.009
Corominas J, Westen C, Frattini P, Cascini L, Malet JP, Fotopoulou S, Catani F, Van Den Eeckhaut M, Mavrouli O, Agliardi F, Pitilakis K, Winter MG, Pastor M, Ferlisi S, Tofani V, Hervás J, Smith JT (2014) Recommendations for the quantitative analysis of landslide risk. Bull Eng Geol Environ 73(2):209–263. https://doi.org/10.1007/s10064-013-0538-8
Cao J, Zhang Z, Du J, Zhang L, Song Y, Sun G (2020) Multi-geohazards susceptibility mapping based on machine learning—a case study in Jiuzhaigou, China. Nat Hazards 102:851–871
de Ferranti J (2015) digital elevation data—with SRTM voids filled using accurate topographic mapping. Digit Elev Data 20–159
Easterling DR, Kunkel KE, Arnold JR, Knutson TR, LeGrande AN, Leung LR, Vose RS, Waliser DE, Wehner M (2017) Precipitation change in the United States. Fourth National Clim Assess I:207–230. https://doi.org/10.7930/J0H993CC
European Space Agency (2017): Land cover CCI product user guide version 2. Tech. Rep
Geoscience Australia (2018): Landslide search. https://pid.geoscience.gov.au/dataset/ga/74273
Guo Z, Ferrer JV, Hürlimann M, Medina V, Puig-Polo C, Yin K, Huang D (2023) Shallow landslide susceptibility assessment under future climate and land cover changes: a case study from southwest China. Geosci Front 14(4):101542. https://doi.org/10.1016/j.gsf.2023.101542
Gariano SL, Guzzetti F (2016) Landslides in a changing climate. Earth Sci Rev 162:227–252. https://doi.org/10.1016/j.earscirev.2016.08.011
Gariano SL, Guzzetti F (2022) In: Shroder JJF (ed) 5.32 - mass-movements and climate change, pp 546–558. Academic Press, Oxford. https://doi.org/10.1016/B978-0-12-818234-5.00043-2
Gründemann GJ, Giesen N, Brunner L, Ent R (2022) Rarest rainfall events will see the greatest relative increase in magnitude under future climate change. Commun Earth Environ 3(1):1–9. https://doi.org/10.1038/s43247-022-00558-8
Hulme M, Barrow EM, Arnell NW, Harrison PA, Johns TC, Downing TE (1999) Relative impacts of human-induced climate change and natural climate variability. Nat 397(6721):688–691
Hughes KS, Bayouth García D, Martínez Milian GO, Schulz WH, Baum RL (2019) Map of slope-failure locations in Puerto Rico after Hurricane María: US Geological Survey data release. US Geological Survey, Reston, VA. https://doi.org/10.5066/P9BVMD74
Handwerger AL, Fielding EJ, Sangha SS, Bekaert DPS (2022) Landslide sensitivity and response to precipitation changes in wet and dry climates. Geophys Res Lett 49(13):1–12. https://doi.org/10.1029/2022GL099499
Hürlimann M, Guo Z, Puig-Polo C, Medina V (2022) Impacts of future climate and land cover changes on landslide susceptibility: regional scale modelling in the val d'aran region (pyrenees, spain). Landslides, 1–20
Handwerger AL, Huang MH, Fielding EJ, Booth AM, Bürgmann R (2019) A shift from drought to extreme rainfall drives a stable landslide to catastrophic failure. Sci Rep 9(1). https://doi.org/10.1038/s41598-018-38300-0
Hartmann J, Moosdorf N (2012) The new global lithological map database GLiM: a representation of rock properties at the Earth surface. Geochem Geophys Geosyst 13(12)
Han Y, Semnani SJ (2024) Important considerations in machine learning-based landslide susceptibility assessment under future climate conditions. Acta Geotech 1–26. https://doi.org/10.1007/s11440-024-02363-3
Huffman GJ, Stocker EF, Bolvin DT, Nelkin EJ, Tan J (2019) GPM IMERG final precipitation L3 1 day 0.1 degree x 0.1 degree V06, Edited by Andrey Savtchenko, Greenbelt, MD, Goddard Earth Sciences Data and Information Services Center (GES DISC). https://doi.org/10.5067/GPM/IMERGDF/DAY/06, https://disc.gsfc.nasa.gov/datasets/GPM_3IMERGDF_06/summary
Juang CS, Stanley TA, Kirschbaum DB (2019) Using citizen science to expand the global map of landslides: introducing the Cooperative Open Online Landslide Repository (COOLR). PloS one 14(7):0218657
Kelkar K, Kirschbaum D, Kirschbaum D, Stanley T (2017) Constructing a comprehensive database for rainfall-triggered landslides in the United States. Geol Soc Am. https://doi.org/10.1130/abs/2017AM-304216
Kirschbaum D, Kapnick SB, Stanley T, Pascale S (2020) Changes in extreme precipitation and landslides over High Mountain Asia. Geophys Res Lett 47(4):1–9. https://doi.org/10.1029/2019GL085347
Knevels R, Petschko H, Proske H, Leopold P, Mishra AN, Maraun D, Brenning A (2023) Assessing uncertainties in landslide susceptibility predictions in a changing environment (Styrian Basin, Austria). Nat Hazards Earth Syst Sci 23(1):205–229. https://doi.org/10.5194/nhess-23-205-2023
Komori D, Rangsiwanichpong P, Inoue N, Ono K, Watanabe S, Kazama S (2018) Distributed probability of slope failure in Thailand under climate change. Clim Risk Manag 20:126–137. https://doi.org/10.1016/j.crm.2018.03.002
Korup O, Stolle A (2014) Landslide prediction from machine learning. Geol Today 30(1):26–33. https://doi.org/10.1111/gto.12034
Kirschbaum D, Stanley T (2018) Satellite-based assessment of rainfall-triggered landslide hazard for situational awareness. Earth's Futur 6(3):505–523. https://doi.org/10.1002/2017EF000715
Lynn E, Schwarz A, Anderson J, Correa M, O'Daly W, Keeley F, Woled J (2015) Perspectives and guidance for climate change analysis. California Department of Water Resources (DWR) Climate Change Technical Advisory Group (CCTAG): August, 142
Lin Q, Steger S, Pittore M, Zhang J, Wang L, Jiang T, Wang Y (2022) Evaluation of potential changes in landslide susceptibility and landslide occurrence frequency in China under climate change. Sci Total Environ 850. https://doi.org/10.1016/j.scitotenv.2022.158049
Mirus BB, Jones ES, Baum RL, Godt JW, Slaughter S, Crawford MM, Lancaster J, Stanley T, Kirschbaum DB, Burns WJ et al (2020) Landslides across the USA: occurrence, susceptibility, and data limitations. Landslides 17:2271–2285
Mudelsee M (2019) Trend analysis of climate time series: a review of methods. Earth Sci Rev 190:310–322
Neelin JD, Langenbrunner B, Meyerson JE, Hall A, Berg N (2013) California winter precipitation change under global warming in the coupled model intercomparison project phase 5 ensemble. J Clim 26(17):6238–6256. https://doi.org/10.1175/JCLI-D-12-00514.1
NOAA PSL: CPC Global Unified Temperature data provided by the NOAA Physical Sciences Laboratory, Boulder, Colorado. https://psl.noaa.gov/data/gridded/data.cpc.globaltemp.html
Ozturk U, Bozzolan E, Holcombe EA, Shukla R, Pianosi F, Wagener T (2022) How climate change and unplanned urban sprawl bring more landslides. Natur 608(7922):262–265. https://doi.org/10.1038/d41586-022-02141-9
Pham QB, Chandra Pal S, Chakrabortty R, Saha A, Janizadeh S, Ahmadi K, Khedher KM, Anh DT, Tiefenbacher JP, Bannari A (2022) Predicting landslide susceptibility based on decision tree machine learning models under climate and land use changes. Geocarto Int 37(25):7881–7907. https://doi.org/10.1080/10106049.2021.1986579
Pierce DW, Das T, Cayan DR, Maurer EP, Miller NL, Bao Y, Kanamitsu M, Yoshimura K, Snyder MA, Sloan LC, Franco G, Tyree M (2013) Probabilistic estimates of future changes in California temperature and precipitation using statistical and dynamical downscaling. Clim Dyn 40(3–4):839–856. https://doi.org/10.1007/s00382-012-1337-9
Pierce DW, Kalansky JF, Cayan DR (2018) Climate, drought, and sea level rise scenarios for California's fourth climate change assessment. California Energy Commission and California Natural Resources Agency CNRA-CEC-2018-006
Park SJ, Dk Lee (2021) Predicting susceptibility to landslides under climate change impacts in metropolitan areas of South Korea using machine learning. Geomatics Nat Hazards Risk 12(1):2462–2476. https://doi.org/10.1080/19475705.2021.1963328
Prein AF, Rasmussen RM, Ikeda K, Liu C, Clark MP, Holland GJ (2017) The future intensification of hourly precipitation extremes. Nat Clim Chang 7(1):48–52. https://doi.org/10.1038/nclimate3168

Rengers FK, McGuire LA, Oakley NS, Kean JW, Staley DM, Tang H (2020) Landslides after wildfire: initiation, magnitude, and mobility. Landslides 17(11):2631–2641. https://doi.org/10.1007/s10346-020-01506-3
Secretaría de Gestión de Riesgos - Escenarios (2016): 2016 Active Events. Technical report. https://sgr-ecuador.carto.com/datasets
Stanley TA, Kirschbaum DB, Benz G, Emberson RA, Amatya PM, Medwedeff W, Clark MK (2021) Data-driven landslide nowcasting at the global scale. Front Earth Sci 9. https://doi.org/10.3389/feart.2021.640043
Stanley TA, Kirschbaum DB, Sobieszczyk S, Jasinski MF, Borak JS, Slaughter SL (2020) Building a landslide hazard indicator with machine learning and land surface models. Environ Model Softw 129:104692. https://doi.org/10.1016/j.envsoft.2020.104692
Shou KJ, Lin JF (2020) Evaluation of the extreme rainfall predictions and their impact on landslide susceptibility in a sub-catchment scale. Eng Geol 265. https://doi.org/10.1016/j.enggeo.2019.105434
Styron R, Pagani M (2020) The GEM global active faults database. Earthquake Spectra 36(1_suppl):160–180. https://doi.org/10.1177/8755293020944182
Shou KJ, Yang CM (2015) Predictive analysis of landslide susceptibility under climate change conditions - a study on the Chingshui River Watershed of Taiwan. Eng Geol 192:46–62. https://doi.org/10.1016/j.enggeo.2015.03.012
Tichavský R, Ballesteros-Cánovas JA, Šilhán K, Tolasz R, Stoffel M (2019) Dry spells and extreme precipitation are the main trigger of landslides in Central Europe. Sci Rep 9:14560. https://doi.org/10.1038/s41598-019-51148-2
Tyagi A, Tiwari RK, James N (2023) Prediction of the future landslide susceptibility scenario based on LULC and climate projections. Landslides. https://doi.org/10.1007/s10346-023-02088-6
U.S. Census Bureau, Department of Commerce (2019): TIGER line shapefile, series information for the primary and secondary roads state-based shapefile
Van Vuuren DP, Edmonds J, Kainuma M, Riahi K, Thomson A, Hibbard K, Hurtt GC, Kram T, Krey V, Lamarque JF (2011) The representative concentration pathways: an overview. Clim Change 109:5–31. https://doi.org/10.1007/s10584-011-0148-z
Wills C, Perez F, Gutierrez C (2011) Susceptibility to deep-seated landslides in California. California Geological Survey map sheet 58
Webb R, Rosenzweig CE, Levine ER (2000) Global soil texture and derived water-holding capacities. Data set available online from Oak Ridge National Laboratory Distributed Active Archive Center, Oak Ridge, Tennessee, U.S.A. https://doi.org/10.3334/ORNLDAAC/548 . Data set available online from Oak Ridge National Laboratory Distributed Active Archive Center. http://www.daac.ornl.gov
Wang Z, Xu S, Liu J, Wang Y, Ma X, Jiang T, He X, Han Z (2023) A combination of deep autoencoder and multi-scale residual network for landslide susceptibility evaluation. Remote Sens 15(3):653. https://doi.org/10.3390/rs15030653

Shabnam J. Semnani (✉) · Yi Han
Department of Structural Engineering, University of California, San Diego, USA
Email: ssemnani@ucsd.edu

Céline J. Bonfils · Joshua A. White
Lawrence Livermore National Laboratory, Livermore, USA